Histol Histopathol (2020) 35: 871-886

http://www.hh.um.es

Histology and Histopathology
From Cell Biology to Tissue Engineering

Growth pattern of experimental glioblastoma

Jonatan Ahlstedt[1]*, Karolina Förnvik[1]*, Gunther Helms[2], Leif G. Salford[1], Crister Ceberg[2], Gunnar Skagerberg[3] and Henrietta Nittby Redebrandt[1,3]*

[1]Rausing Laboratory, Division of Neurosurgery, Department of Clinical Sciences Lund, Lund University, [2]Medical Radiation Physics, Department of Clinical Sciences Lund, Lund University and [3]Department of Neurosurgery, Skåne University Hospital in Lund, Lund, Sweden

*Contributed equally

Summary. Glioblastoma multiforme (GBM) is an aggressive primary brain malignancy with a very poor prognosis. Researchers employ animal models to develop potential therapies. It is important that these models have clinical relevance. This means that old models, propagated for decades in cultures, should be questioned. Parameters to be evaluated include whether animals are immune competent or not, the infiltrative growth pattern of the tumor, tumor volume resulting in symptoms and growth rate. We here describe the growth pattern of an experimental glioblastoma model in detail with GFP positive glioblastoma cells in fully immune competent animals and study tumor growth rate and tumor mass as a function of time from inoculation. We were able to correlate findings made with classical immunohistochemistry and MR findings. The tumor growth rate was fitted by a Gompertz function. The model predicted the time until onset of symptoms for 5000 inoculated cells to 18.7±0.4 days, and the tumor mass at days 10 and 14, which are commonly used as the start of treatment in therapeutic studies, were 5.97±0.62 mg and 29.1±3.0 mg, respectively.

We want to raise the question regarding the clinical relevance of the outline of glioblastoma experiments, where treatment is often initiated at a very early stage. The approach presented here could potentially be modified to gain information also from other tumor models.

Offprint requests to: Henrietta Nittby Redebrandt, Rausing Laboratory, Division of Neurosurgery, Department of Clinical Sciences Lund, Lund University, SE-221 85 Lund, Sweden. e-mail: henrietta.nittby@med.lu.se

DOI: 10.14670/HH-18-207

Key words: Glioblastoma, Rat, Imaging, GFP

Introduction

Glioblastoma multiforme (GBM, WHO astrocytoma grade IV), is an aggressive and today incurable primary brain malignancy with a 5-year survival of less than 5% (Oghaki and Kleihues 2005; Ahmad and Malik, 2017). Murine GBM models have been important for exploration of tumor behavior and investigations of different treatment modalities since the mid-20th century, and many models exist today, several of which are described in a review by Barth and Kaul, 2009. They concluded that each tumor model has its limitations, and that it is essential to choose a model that is well suited for the study in question. It is important to understand the spatial and temporal development of the experimental glioblastoma in order to comprehend the consequences of the timing of the treatment. If the treatment is initiated in an early phase of the tumor development, there may be very little tumor mass to treat, with questionable clinical relevance as a result. The immune competence status of the animals used and the immunogenicity of the tumor model applied are also an important factors, not least when studying immune therapies.

Recent studies using hetero- and xenotransplantation as well as solely *in vitro* research have provided vital information regarding various mechanisms of fundamental importance for our understanding of tumor biology (Tamase et al., 2009; Liu et al., 2011; Duran et al., 2016) and owe much of their value to the possibility of selectively manipulating specific factors. However,

these studies tend to disregard the genetic and functional heterogeneity of these tumors and their multifarious interactions with the host, which is probably at the root of the clinical problem (Hambardzumyan et al., 2016). While the immunological complexities induced by hetero- and xenotransplantation (Liu et al., 2011) are obvious, the tendency for tumor cells grown *in vitro* to become progressively more homogenous (Lampson 2013; Stylli et al., 2015) seems often not to be considered. Accordingly, the chemically induced tumor model in conjunction with the *in vivo* allotransplantation model may still be advantageous and possibly be more appropriate for studying the complex interactions related to host tumor interaction, e.g. in terms of matrix/tumor relations.

Besides the better possibility of controlling for single parameters related to tumor growth or defense, another reason for utilizing the *in vitro* or heterotransplantation method probably resides in the fact that under such circumstances the identification of tumor cells is often facilitated. In the orthotopic allotransplantation *in vivo* model on the other hand, the difficulty of discriminating tumor cells from reactive cells in the vicinity of the tumor, detecting single migrating tumor cells far away from the main tumor mass and vice versa, and to readily discern non-tumor cells invading the tumor in the model, represent an old problem (Mc Lendon et al., 1998). It would thus in many instances be of advantage if the tumor model in some way exhibited a specific feature allowing for positively discerning tumor cells, including potentially tumor-initiating cells (TICs).

The recently introduced nitrosurea induced NS-1 rat tumor model possesses this property and in addition exhibits several of the typical molecular changes seen in glioblastoma (Nittby et al., 2015). By utilizing this model, in which tumor cells express the Green Fluorescent Protein (GFP), for orthotopic allotransplantation to animals of the same strain but devoid of GFP expression, single tumor cells can be detected using conventional immunohistochemistry.

The concept of utilizing GFP as a marker in various brain tumor models is not new and has been profitably used before (Liu et al., 2011; Chen et al., 2012) but the presently described model appears to confer additional advantages. Two such major advantages are that 1) most tumor cells express GFP, and that 2) the tumor cells can be administered to fully immune competent animals without any *ex vivo* manipulation.

In this report, we further explore the development of untreated NS1 tumors in fully immunocompetent animals. For this purpose, we established magnetic resonance imaging (MRI) protocols *in vivo* and *post mortem* and compare the tumor characteristics seen by imaging with histological examinations. We also explore the effect of the number of grafted cells upon time until onset of symptom (OS) and set up a mathematical model to calculate the tumor growth rate and the tumor mass as a function of time from inoculation. Furthermore, we use MRI with a gadolinium-based contrast agent (CA) to depict alterations of the blood-brain barrier, a common feature of pathological tumor vascularization (Drean et al., 2016; Sourbron and Buckley, 2013), and study the immunogenicity of the developing tumor by using immunohistochemical staining for CD8, CD4 and FoxP3. We also demonstrate the morphological characteristics and discuss the methodological possibilities of this tumor model.

Materials and methods

Ethics statement

This study and the procedures described were approved by the animal ethics committee in Lund, with permit ID M15-16 and M128-14 (Nittby Redebrandt). Every effort was made to reduce animal suffering.

Cell line

The NS-1 tumor cell line was established from an intra-parenchymal tumor growing in the pons in the offspring of a pregnant homozygous GFP-positive Fischer rat treated with ethylnitroso-urea as described previously (Nittby et al., 2015). The tumors are positive for GFAP, GFP, and the cells have been shown to have a strong RNA expression for wt *IDH1*, wt *p53*, *IDO1* and *EGFR*. The detection of GFP in the tumor cells was evaluated *in vitro* using a fluorescence microscope, and the NS1 cells demonstrated GFP fluorescence prior to inoculation.

Animals

Fischer 344 rats were purchased from Fischer Scientific. Endpoints were defined by symptoms of brain tumors, such as paresis, seizures, or poor general condition. Rats were monitored daily with respect to these symptoms, all of which prompted euthanasia. Rats were housed in hutches with enriched environments in groups of two or three with *ad libitum* access to food and water.

A total of 18 rats that had received 5000 NS-1 cells were included. In another 11 animals, larger cell amounts were used (50 000 cells n=4, 100 000 cells n=3, 200 000 cells n=2 and 300 000 cells n=2) to evaluate the relationship between inoculation dose and time to symptoms. Furthermore, 11 rats were used to replicate the results with 5000 cells, but with NS1 cells from later passages of the cell line.

All rats received stereotactic tumor inoculation into the right caudate nucleus (C). To establish intracranial tumors, the required numbers of cells were suspended in 5 µl of R0 medium. As described previously (Nittby et al., 2015; Förnvik et al., 2017; Ahlstedt et al., 2018), inoculations were performed using a 10 µl Hamilton syringe mounted on a stereotactic frame. The cell suspension was injected through a burr hole placed 2

mm lateral and 1 mm anterior to the bregma, at a depth of 5 mm. The suspension was injected at a pace of 1 µl/min, with a 5-minute pause before retraction at a pace of 1 mm/min. Anesthesia was achieved with continuous isofluorane inhalation during the entire surgical procedure. The burr hole was sealed with bone wax and the wound sealed with resorbable suture.

Immunohistochemistry for morphology and GFP detection

After 11 days survival, the apparently still healthy, normally functioning animals were sacrificed under deep carbondioxide anaesthesia. The animals were first perfused with 100 ml of 4C PBS followed by 200 ml of 4% formaldehyde at the same temperature. The brains were dissected and 3-5 mm thick, coronally cut slabs, visually confirmed to contain the implanted tumor, were then after-fixed for 24h at room temperature.

Following fixation, the tissue slabs were embedded in paraffin and cut in the coronal plane in series at 7 um. After being mounted on glass slides the sections were deparaffinized and every fifth stained with Hematoxylin/Eosin (H/E). Adjacent sections were subjected to antigen retrieval by microwave irradiation for 1min while immersed in citrate-buffer. Individual sections were incubated with polyclonal antibodies against GFP for two hours. The GFP antibody was biotinylated and raised in goat (ABIN 10087). The bound primary antibody was visualized using appropriate biotinylated secondary antibodies and ABC-reagent using a ready to use Vectastain Elite® ABC kit (Vector Laboratories, CA, USA). Finally the ABC-complex was visualized utilizing the Dako® Chromogen system (Dako H3467). Some of the sections processed for visualization of GFP were lightly counterstained with H/E subsequent to the completion of the immunohistochemical procedure. Sections were mounted on slides, embedded in Permount® and coverslipped.

The results were analyzed using a standard Olympus® Light-microscope equipped with standard objectives and an infinity 2-C (lumenera®) camera for photographic documentation. The obtained pictures were annotated by adding symbols and scale bars (Windows Paint®) but not manipulated in any other way.

Immunohistochemistry for CD4, CD8 and FOXP3 detection

After 18 days survival, the apparently still healthy, normally functioning animals were sacrificed under deep carbondioxide anaesthesia. Immediately after euthanasia, brains were removed and immersed in 4% w/v formaldehyde for a minimum of 5 days. Frozen sections were serially cut into 40 µm slices focused at the location of the maximum tumor diameter in the coronal plane and stained with haematoxylin-eosin. Other sections were incubated with a rabbit monoclonal antibody against GFP (Antibodies online) at a dilution of 1:200 and subsequently treated with a biotinylated secondary antibody and ABC reagent 30 minutes each, using a ready-to use Vectastain ABC kit (Vector Laboratories®, CA, USA). The antigen-antibody complex was visualized using the DAKO Liquid DAB Substrate-Chromogen System (DAKO®, CA, USA). When the tumor cells were visualized using a fluorescent microscope, the brain was perfused with saline and formaldehyde, and fixated only overnight in 4% formaldehyde, after which frozen sections were serially cut and placed immediately in a microscope. Other sections were incubated with CD4 (Sigma-Aldrich®), CD8 (Antibodies online®) and FOXP3 (Antibodies online®) at a dilution of 1:100 (anti-CD4, anti-CD8, FOXP3) overnight and subsequently treated with a biotinylated secondary antibody and ABC reagent 30 minutes each, using a ready-to use Vectastain ABC kit (Vector Laboratories®, CA, USA). The antigen-antibody complex was visualized using the DAKO Liquid DAB Substrate-Chromogen System (DAKO®, CA, USA).

Magnetic resonance imaging

MRI was performed on 5 rats using a 3T clinical whole-body MR system (Magnetom Prisma, Siemens Healthcare, Erlangen, Germany) and a wrist coil (Invivo, Gainesville, FL, USA; using eight carpal of 16 receive elements). Prior to imaging, rats were anesthetized using ketamine at a dose of 60 mg/kg i.p. which maintained sedation during the entire procedure. The animals were placed in supine position with the skull centred in the carpal region of the coil and scanned under free breathing at an ambient temperature of 21°C. Body temperature was maintained during the scan by wrapping the body extremities in a soft tissue towel, which also restrained motion. Breathing and motion during the examination were controlled visually. The MRI examination lasted 40 minutes in total. For contrast-enhanced MRI, 0.1 ml of 0.5 M gadobenate dimeglumin (MultiHance® Bracco Imaging, Milano, Italy) was administered in two animals on day 14 by intraperitoneal injection amounting to a dose of approximately 2.8 mmol/kg body weight for the studied rats.

Imaging volumes were acquired with three-dimensional (3D) spatial encoding with the read-out direction along the body axis of the animal (128 mm field-of-view (FoV)) at a resolution of three pixels (px) per mm), as described previously (Helms et al. 2013). The FoV in phase and partition direction was chosen as small as possible (phase: 52 mm or156 px; partition: 43 mm or 128 px) to constrain the measurement time.

For T1-weighted structural MRI with and without CA, a magnetization-prepared rapid acquisition of gradient echoes (MP-RAGE) sequence was used with the parameters recommended for human brain at 3T (inversion time TI=0.9 s, non-selective read-out of 128 partition-encodings at flip angle 9°, echo time TE=2.61

mm (37% asymmetric echo with a bandwidth of 330 Hz/px repeated every 11.8 ms. The total repetition time TR was 2.3 s, as has been described (Jack et al., 2008). Two blocks (each of 2 averages, 8:48 min) were acquired.

T2-weighted MRI was performed using a 3D turbo spin-echo (TSE) sequence with variable refocusing flip angles [with phase partial Fourier, slice turbo factor 2, GRAPPA (general autocalibration for parallel partial acquisition) factor 2 with 24 reference lines]. The read-out bandwidth of 334 Hz/px imposed an echo spacing of 7.12 ms and an effective TE of 235 ms. Three blocks (each of two averages 6:45 min) were acquired.

Data processing

DICOM images (digital imaging and communications in medicine) in the radiological right-left convention were converted to 3D NIFTI image volumes (neuroimaging informatics technology initiative) complying with the neuroscience left-right convention.

Image registration by 6 parameter rigid body transform was performed using FLIRT (FMRIB's Linear Registration Tool) as provided in the FSL software library of the Centre for Functional Magnetic Resonance Imaging of the Brain (FMRIB, University of Oxford, UK, www.fmrib.ox.ac.uk/fsl version 5.0.8).

First, one T1-weighted image volume was registered to an axial rat template at 250 µm isotropic resolution. Subsequently, all other image volumes were registered to this volume (individual template) to achieve a consistent angulation despite individual positioning and animal movements. Finally, the image volumes that were free of motion artifacts were averaged to increase the signal-to-noise ratio (SNR).

MRI volumetric measurements

3D regions-of-interest (ROI) of the tumors (excluding peri-tumoral edema) were outlined by hand on T2-weighted images using the MRIcro Viewer version 1.40; C. Rorden, Columbia, SC (people.cas.sc.edu/rorden/mricro/index.html). The volume of each ROI was calculated from the number of pixels.

Contrast agent uptake

The uptake of CA was studied in two rats with intracranial NS-1 tumors on day 14 post inoculation. Contrast changes were monitored at intervals of 15

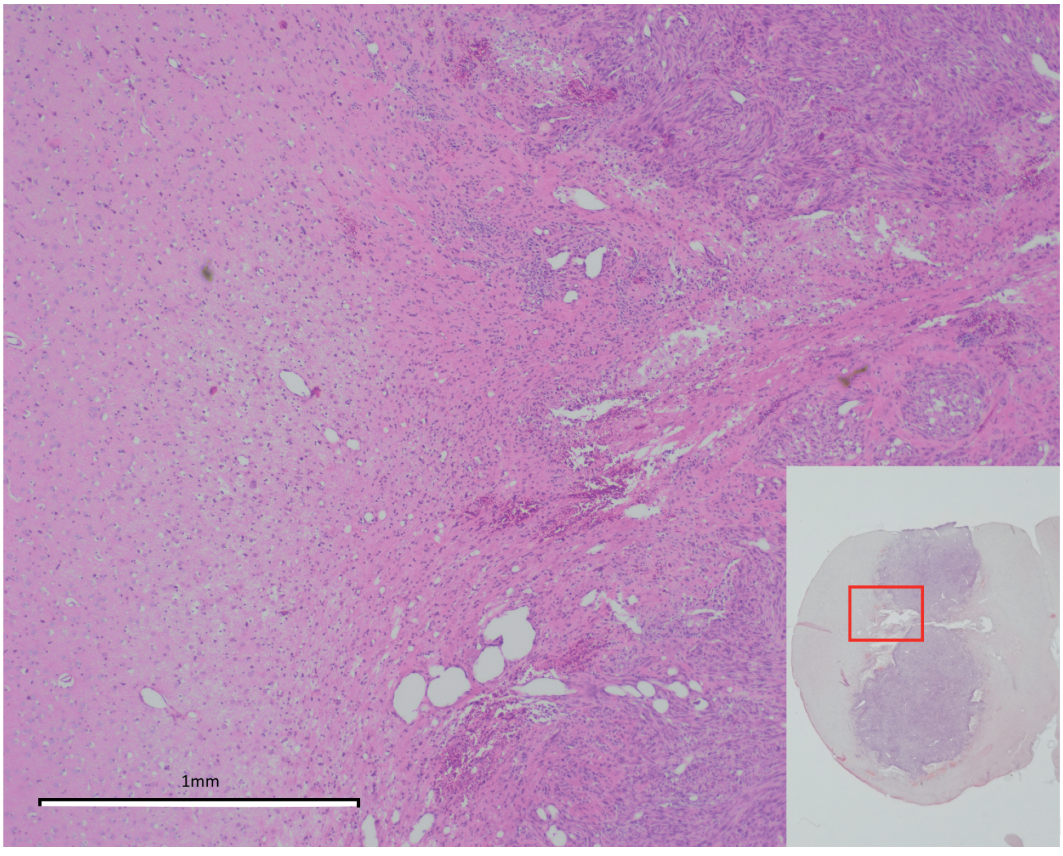

Fig. 1. Overview image of tumor 18 days after inoculation of 5 000 cells into the right caudate nucleus. The tumor grows in an expansive way, infiltrating into the brain tissue at the tumor borders, which is further magnified in the framed area.

minutes by four additional T1-weighted volumes of 3 averages after CA administration. ROIs were placed in the tumor center and in the jaw muscle, which served as reference region without blood-brain barrier.

High resolution MRI

To underpin the interpretation of low-resolution MRI *in vivo*, two brain specimens were perfusion-fixed in 4% buffered formaldehyde (14 days after inoculation of 5000 cells) and scanned at 9.4T using an animal MR scanner equipped with a superconducting cryocoil (Bruker Biospin, Ettlingen, Germany). Image sets of 45 μm resolution were acquired by a 3D FLASH (fast low-angle shot) sequence with TR/TE/FA=40 ms/16 ms/10° yielding a predominantly T2*-weighted contrast, which is particularly sensitive to hemoglobin and breakdown products.

Results

Immunohistochemical analyses of tumor morphology and invasiveness

The primary site of tumor implantation could be directly seen already in the dissected coronal slabs, as seen in Fig. 1, where an overview of the tumor 18 days after inoculation of 5,000 cells is presented. The tumor edge grows in an infiltrative manner. The growth patterns were further explored in the animals at day 11 post inoculation. Also in these animals, the main tumor and larger satellites were, in the H/E stained sections at low magnification, easily identified as distinctly stained hypercellular areas. The main bulk of tumor was found at the expected site within the central area of the caudate nucleus (C) beneath the corpus callosum (cc) corresponding to the implantation site. The tumor was often observed along the needle track through the cortex sometimes with local spread in the subarachnoid space on the cortical surface and in all cases disseminated aggregates of tumor cells could be detected already at lower magnification, several mms from the main tumor mass (Fig. 2A). The central area of the tumor appeared to consist of often tightly packed tumor cells and frequently exhibited signs of neovascularization as well as areas of necrosis (Fig. 2B,D,G). The size of the main tumor at the site of implantation was clearly related to the number of cells implanted and this main bulk of the tumor exerted a variable expansive and compressive effect on the adjacent lateral ventricle and to some extent also on the anterior portion of the third ventricle.

At higher magnification the salient features of glioblastoma were readily seen; neovascularization, necrosis, sometimes with pseudopallisading, cellular pleomorphism and nuclear atypia (Fig. 2C,E,H). Mitotic figures, often of clearly aberrant type (Fig. 2C) and signs of bleeding were frequent in some parts of the tumors (Fig. 2H). Within the parenchyma the invasiveness was prominent with tumor spread observed in all directions although penetration of pia mater or the ependymal lining only appeared in restricted areas (Fig. 2B,D,G). Signs of neovascularization were seen in all but the smallest tumors. While, especially in areas with necrosis, formation of microcysts could sometimes be mistaken for vascular proliferation, the latter process, due to the relatively high pressure required for adequate perfusion, was usually evidenced by an increased number of distinctly ballooning vessels (Fig. 2E), in which only occasionally red blood cells (RBCs) remained after wash-out (Fig. 2H). The tumor sometimes appeared in typical glomeruloid arrangements, with densely packed tumor cells located around a more central vessel.

Intratumoral bleeding as evidenced by extravascular erythrocytes was a common but not conspicuous feature (Fig. 2H). Accumulations of small numbers of tumor cells close to intraparenchymal vessels distant from the main tumor were common, but in H&E staining difficult to distinguish from perivascular aggregations of lymphocytes.

Occasionally, clusters of tumor cells were observed "free" in the ventricles (V) (Fig. 2F). These clusters usually had a distinct "spheroid" appearance in which the cells often appeared more uniform with less pleomorphism than in intraparenchymal tumors of similar size.

Despite the circumscript appearance of the tumors at low magnification the border zone was always blurred and exhibited a substantial number of cells that in H&E staining could not be readily classified as either tumor or non-tumor (Fig. 2B,D).

The immunocytochemical method employed resulted in a distinct brown staining (GFP+) that seemed to completely fill the tumor cells, sometimes with an accentuated staining corresponding to the nucleus (Fig. 3E,F). The degree of immunostaining of tumor cells varied only slightly and the "cut off" from host non GFP expressing tissue (GFP-) was quite distinct (Fig. 3B,E). Thus, background staining was virtually absent within the normal parenchyma (GFP-) and neither was any unspecific immunocytochemical staining seen within the meninges or in the ependymal or pial lining (Figs. 4B, 5B,C). The process of counterstaining the immunocytochemically processed sections somewhat changed the hue of the GFP+ to a more red-brown color but in no way decreased contrast (Fig. 3C,F). Since the GFP staining tended to obscure cytological detail it was found useful to compare closely situated, if possible adjacent, sections stained with H&E alone or in combination with staining for GFP for cytological and anatomical detail which greatly facilitated the interpretation – although, with the section thickness used, it did not usually allow for comparison of individual cells (Fig. 4H,I). Especially close to the site of implantation, the tumor cells formed continuous sheets of closely packed GFP+ cells with interspersed GFP- cells becoming progressively more frequent with increasing distance from the implantation site.

While this technique confirmed the general

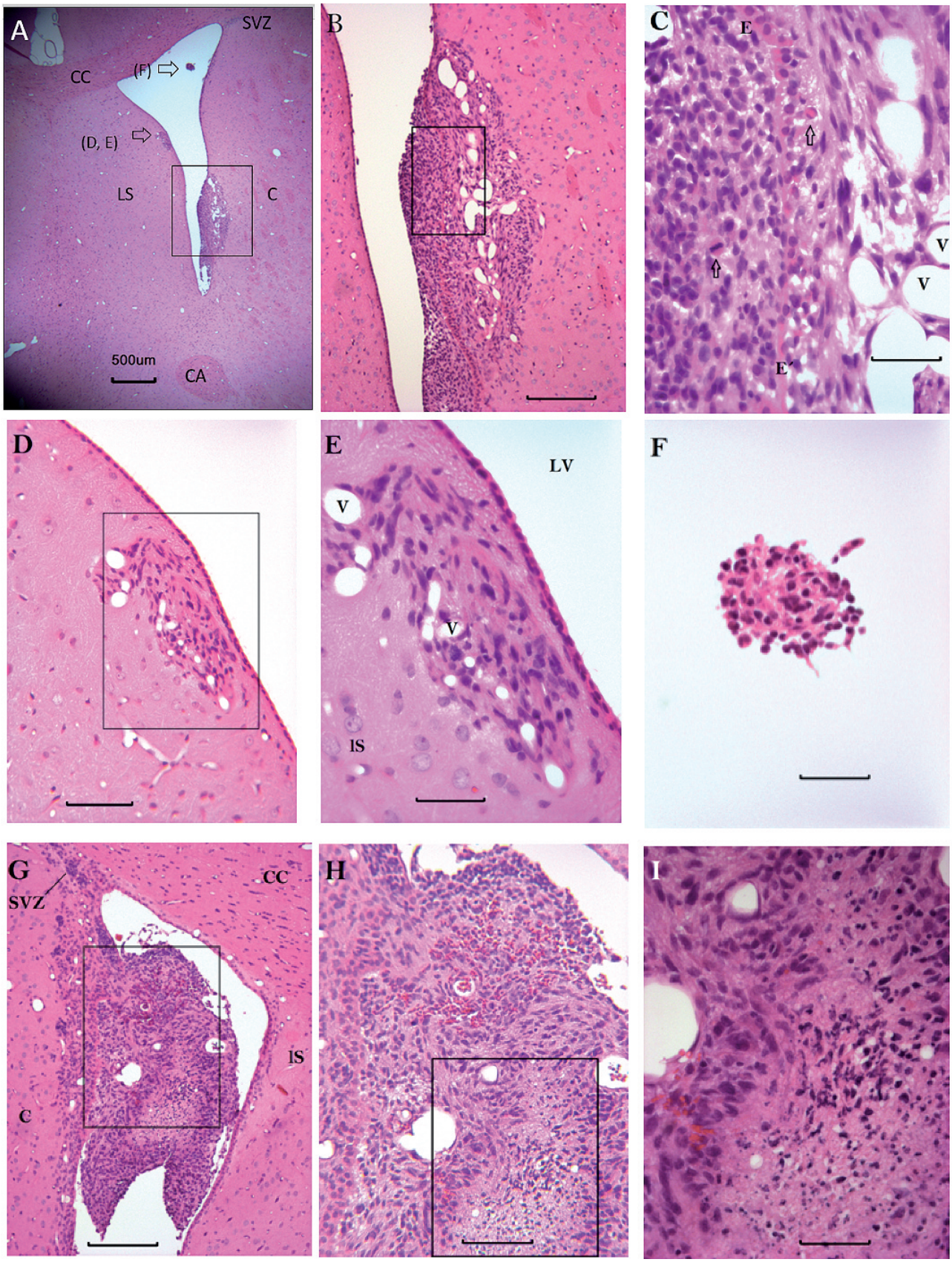
A
SVZ
CC
(F)
(D, E)
LS
C
500um
CA
B
C
E
V
V
E'
D
E
LV
V
V
lS
F
G
SVZ
CC
lS
C
H
I

impression of spread in the vicinity of individual tumor masses seen already in the H&E stained material, the combined method also disclosed unsuspected and otherwise easily missed spread of small numbers of tumor cells both within the parenchyma far from the more obvious tumor sites (Fig. 4B,D-F) and also within the subarachnoidal space, including the ventricular compartment. These small groups of tumor cells often had an appearance that was not distinctly abnormal, although, when closely adjacent H&E sections were scrutinized, suspects were most often detected. Usually, however, these were revealed by their higher cell density and abnormal location rather than by distinctly aberrant morphology of single cells. In no case did we, in the H&E only sections, encounter morphologically deviant cells whose counterparts in the adjacent GFP stained section were not GFP-positive. Thus, in all cases when adjacent sections stained for GFP were available, cells that were deemed as tumor suspects in H&E were confirmed as such by similarly located GFP+ counterparts in nearby sections (Figs. 4G-I, 5A,B). Accordingly, in all cases in which we in the H&E only sections encountered arrangements of cells that appeared tumor-suspect we could, when the corresponding area was scrutinized in adjacent sections stained for GFP, find cells containing this marker thus proving their tumorous identity. In contrast however we sometimes observed singular distinctly GFP+ cells, which could not on morphological grounds only, be identified as tumor cells in adjacent H&E only sections.

With the combined stain, the reversed situation - of intermixed GFP- cells within areas of densely packed GFP+ cells - was a prominent finding, expected but not readily hinted at from the impression obtained by H&E stain only (Fig. 3D,F). Although not systematically investigated, the general impression was that GFP- cells, probably representing host macrophages and lymphocytes, were less frequent within intraventricular isolated "spheroid" aggregations of tumor.

Detection of CD4, CD8 and FOXP3

Immunohistochemical staining for CD4, CD8 and FoxP3 is presented in Fig. 6. Infiltration of both CD4, CD8 and FOXP3 positive cells could be demonstrated mainly in the tumor border zone, but not in the center of the tumor, and not in the rest of the brain.

Survival data

Initial inoculations with high cell counts (50 000 cells n=4, 100 000 cells n=3, 200 000 cells n=2 and 300 000 cells n=2) yielded OS ranging from 13 to 16.3 days, increasing as doses were lowered. Lowering doses to 5000 cells resulted in OS of 20.9±3.2 days (Fig. 7), leaving approximately 10 to 14 days, with some variability, for treatment to be administered to animals. No animals failed to develop tumors. Replication of the inoculations with 5000 cells from later passages of the cell culture resulted in OS of 19.3±2.5 days (n=11). We could not demonstrate any change in the growth pattern of the tumor as a result of increased number of inoculated cells; time until development of symptoms was the only factor which was affected. Tumors develop fast with this model, which is to be compared to patient derived xenograft models, where it can take 2-11 months for tumors to develop, engraftment might be unsuccessful and a large heterogeneity might confound the picture (Kijima and Kanemura, 2017).

Magnetic resonance imaging and tumor volumetry

T2-weighted images provided clearer distinction of tumor mass than T1-weighted images, as expected. A hypointense rim can be clearly distinguished from the hyperintense edema surrounding the tumor. The CA-enhanced T1w images show the dynamics of contrast uptake, which was homogeneous across the tumor center visible on T2w MRI and reached a broad maximum

Fig. 2. H&E stained sections illustrating the general morphological feature of the NS-1 tumor. **A.** Low-power, coronal plane, overview visualizing cellular aggregates representing three different types of tumor spread (arrows) about 2 mm away from the main tumor injection site. Already at low magnification the tumors are readily recognized by their increased cellular density. The framed area is further magnified in B. The areas indicated by arrows D, E and F are magnified below in Fig. 2D,E,F. **B.** At medium power magnification the lower tumor in Fig. A appears circumscribed but with variable cellular packing and the invasiveness witnessed by tumor breaking through the ependymal lining. The framed area is further magnified in C. **C.** At high magnification the cellular pleomorphism is apparent as well as some microcystic formation and, particularly prominent, neovascular profiles (V). The ependymal lining (E) is deformed and displaced. Arrows point to mitotic figures. **D.** Periventricular tumor growing in the lateral septum but leaving the ependymal lining intact. The cellular density is lower than in B but still easily recognizable together with the increased number of vascular profiles. The framed area is further magnified in E. **E.** At higher magnification especially the often increased staining and variable shape of the atypical nuclei are shown. **F.** An apparently "free-floating" aggregate of intraventricular tumor forming a "sphere" composed of rather uniform cells and intercellular "matrix". **G.** At a similar coronal level on the other side of the brain a tumor growing both in the parenchyma and intraventricularly is shown apparently displacing the small intensely stained aggregates of cells belonging to the subventricular zone compartment and which are difficult to separate from small cells of the tumor. **H.** At higher magnification tumor penetrating the ependyma is seen in the upper part of the picture where close to the ventricular surface small intensely stained cells are seen that could represent either tumor or SVZ cells. Some of the vascular profiles contain red blood cells. Pseudopallissading is shown around the necrotic area within the outlined rectangle. **I.** At high power the cellular and nuclear polymorphisms is readily visualized as is the cellular debris and incipient formation of microcysts in the necrotic area. CA, Anterior cingulate area; C, caudate nucleus; cc, Corpus callosum; IS, Lateral septum; SVZ, Subventricular Zone. Scale bars: A, B, D, G, 200 μm; C, E, I, 50 μm; H, 100 μm.

between 20 and 30 minutes after administration. At time point 4 the contrast enhancement persisted predominantly outside the rim, which may be explained as a combined effect of diffusion into the increased extra-cellular space and poor elimination (Fig. 8).

Selected cross sections of MR volumes are displayed for each of the rats in Fig. 8. The tumor burden demonstrated by MRI fitted well to the corresponding histological volume demonstrated in the sections (Fig. 9D,E). On day 7 across all three examined animals, no clearly visible tumor mass could be identified at the injection site.

High resolution MRI of fixed brains

The iron-sensitive T2*-weighted MRI (Fig. 10)

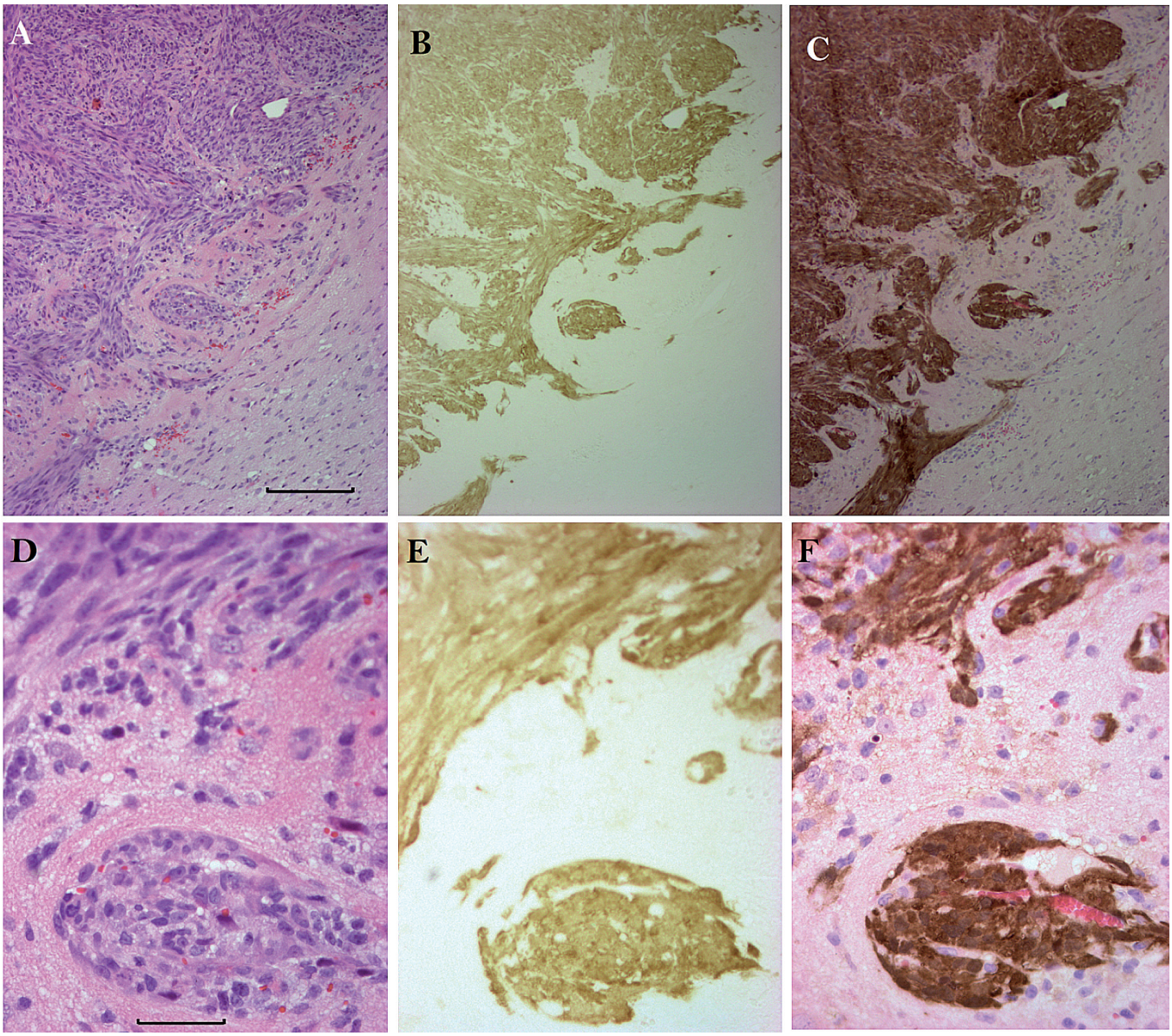

Fig. 3. A-C. Illustrates the appearance of the border zone between a solid tumor area (upper left corner) and normal surrounding brain parenchyma (lower right corner) in semi-adjacent sections stained with H&E **(A, D)**, with antibody to GFP **(B, E)** and with a combination of these **(C, F)**. For reference there is a glomeruloid tumor formation just below the center of the picture and a rather large empty probably vascular structure half way off center to the right in the upper part. **D-F.** Show the central area at higher magnification which reveals the very low background with staining for GFP **(E)** while good contrast is maintained with the combination stain **(F)**. Since the sections are adjacent rather than identical individual cells cannot be compared but the pattern of tumor spread is clearly shown. Scale bars: A-C, 200 μm; D-F, 50 μm.

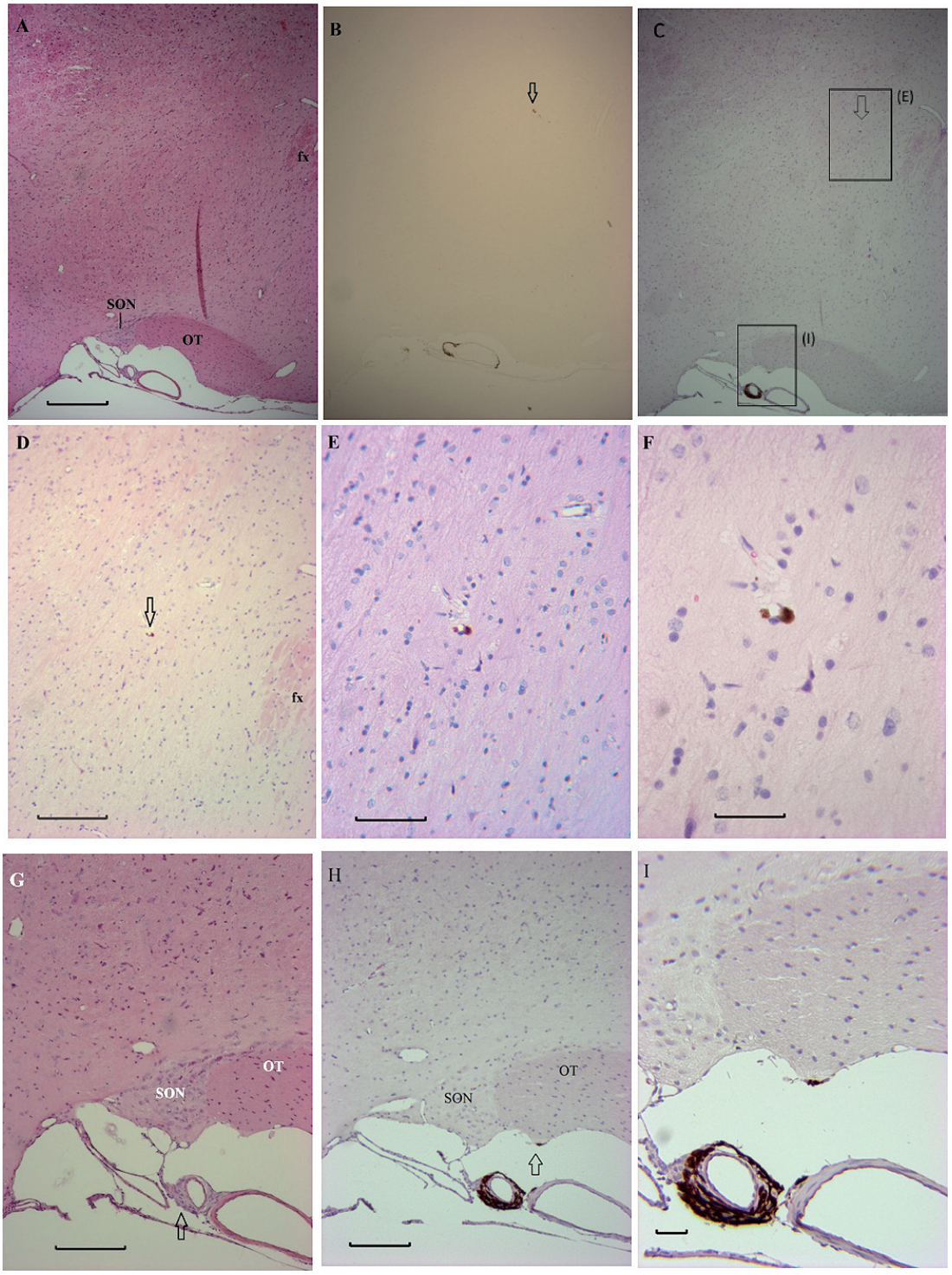

Fig. 4. Demonstrates the distant spread of GFP+ tumor cells in the brain parenchyma and in the tissues of the subarachnoidal space several mm from location of the main tumor. **A-C.** At low power semi-adjacent sections stained with H&E, visualizing GFP+ only and a combination thereof respectively. In A the optic tract (opt) and the supraoptic nucleus (SON) and the fornix (fx) allows for anatomical reference while the presence of tumor cells is not immediately obvious. In B the anatomical structures are hard to discern, because of the high specificity with almost no specific background staining. The presence of GFP+ positive cells is indicated both in the vascular structure below the SON, and within the dorsal hypothalamus (arrow) and the same location of GFP+ cells can also be observed in C, at least when using B as reference. The framed areas in Fig. 4C correspond to the magnifications seen in Fig. 4D,I. **D-F.** Single GFP+ cells within the upper frame in C at successively higher magnifications. **G.** At medium magnification in a H&E stained section through the basal hypothalamus the arrow points to a hypercellular thickening of the vascular structure in the subarachnoidal space. **H.** With the combination staining the same cells are clearly GFP+ as are also one or two cells at the pial surface of the opt (arrow). **I.** At higher magnification individual GFP+ cells are seen, also in the wall of the nearby vein. Scale bars: A-C, 400 μm; D, G, H, 200 μm; E, 100 μm; F, I, 50 μm.

confirmed the presence of macrophages in the hypointense tumor rim. The hypointense rim was irregular but the compact tumor shape still warrants low-resolution MRI for *in vivo* volumetry as partial volume effects will cancel out. In the corpus callosum, the jagged border demonstrated infiltration along the axonal tracts. Homogeneous contrast in the center (approximately isointense with adjacent cortex) indicated high cellularity and absence of necrotic voids.

Tumor mass as a function of time after inoculation

Both the MR-images and the survival data yielded important information concerning the tumor growth characteristics. While the MR-images gave direct measures of the tumor mass W at different time points, the survival data represented the time until OS leading to euthanasia, which was assumed to occur when the tumor had reached a critical mass W sympt. In order to obtain a common interpretation of these two data sets, we employed a Gompertz growth model, reparametrized according to Tjørve and Tjørve (2017), describing the tumor mass as a function of time t after inoculation:

$$W(t) = A\left(\frac{W_0}{A}\right)^{\exp(-kt)}$$

In Equation, W_0 is the initial tumor mass, A is the asymptotic maximum value, and k is a growth rate coefficient. The initial mass was calculated as $W_0=Nw$, where N is the number of inoculated cells and w is the average weight of a single tumor cell. Thus, the model had four free parameters, see Table 1, which were fitted to the available survival times and tumor growth data by the least square method, with an additional penalty on the deviation from the initial estimates, using the lsqnonlin-function in Matlab. In order to estimate the variance of the model, the fit was repeated 10,000 times with the data for each experimental treatment group resampled using bootstrapping with replacement.

The fitted model is shown together with the experimental data in figs. 11 and 12. The time until OS leading to euthanasia for varying number of inoculated cells is shown in Fig. 11, and the tumor mass at different time points after inoculation is shown in Fig. 12. The model predicted the time until onset of symptoms for 5000 inoculated cell to 18.7±0.4 days, and the tumor mass at days 10 and 14, which are commonly used as the start of treatment in therapeutic studies, were 5.97±0.62 mg and 29.1±3.0 mg, respectively.

Discussion

In summary, we here demonstrate the spatial and temporal growth pattern of an infiltrative glioblastoma in untreated animals, in particular the exponential

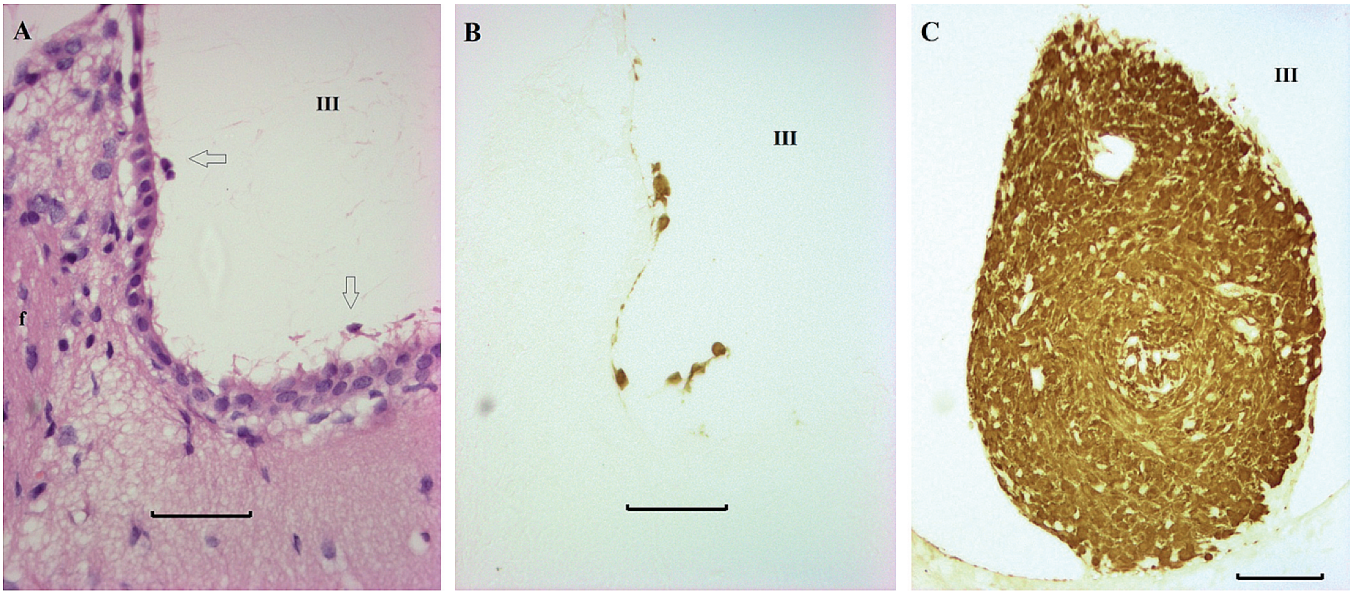

Fig. 5. Demonstrates the high specificity and sensitivity of the present method as shown in cases of intraventricular dissemination of tumor. The cells were inoculated into the right caudate nucleus with the same entry and target point as used in the other animals. **A.** In a H&E stained section through the anterior tip of the third ventricle (III) a few aberrantly located cells close to the ependymal lining are noticed. **B.** In an adjacent section antibody to GFP revels cells in a similar location thus strongly arguing for the atypical cells in A as being tumor cells. Note the very low background and complete absence of GFP+ structures in the parenchyma. **C.** A large "spheroid" accumulation of GFP+ positive cells within the bottom part of the third ventricle. A few cells appear to adhere to or infiltrate the ependymal lining of the ventricle, which can be barely discerned, while no GFP- positivity can be found in the surrounding parenchyma. Scale bars: A, B, 50 μm; C, 200 μm.

expansion of tumor burden over time, the infiltrative growth as seen with immunohistochemistry, and the tumor distribution at the onset-of-symptoms. Formulas to calculate tumor growth have been presented, which could be of use also in other models, given that the relevant parameters are provided. We mean that this could be a useful tool when trying to plan relevant experimental studies. Translation of conclusions made from these formulas to the clinical setting is of course difficult to make. Advanced attempts to make calculations on glioblastoma models have been presented by Rutter et al., 2017, where the authors explored the large variances in final tumor size in a mouse glioblastoma model. Nevertheless, the Gompertz growth model has been useful to calculate tumor mass as a function of time from the initiation of tumor growth in the clinical setting (Stensjoen et al., 2018). With this model it could be estimated that the median age of the tumor at diagnosis was 330 days, with a range from 156 days to 776 days, depending on the tumor volume at diagnosis. The same growth model was also used to calculate the impact of extent of resection on gained survival time. The idea of using GFP as a tumor marker is not new and has been profitably used in many studies (Hoffman, 2015; Endaya et al., 2016). Usually, however, these methods have aimed at visualizing a defined subpopulation of the tumor by coupling its expression to a promotor selected because of its relation to a certain cellular state and most often applied to murine tumors induced by genetic engineering and thereby exhibiting a few, though well defined, genetic alterations (Marumoto et al., 2009; Tamase et al., 2009; Liu et al., 2011; Sampetrean et al., 2011; Chen et al., 2012; Stylli et al., 2015). In contrast, the presently described method takes

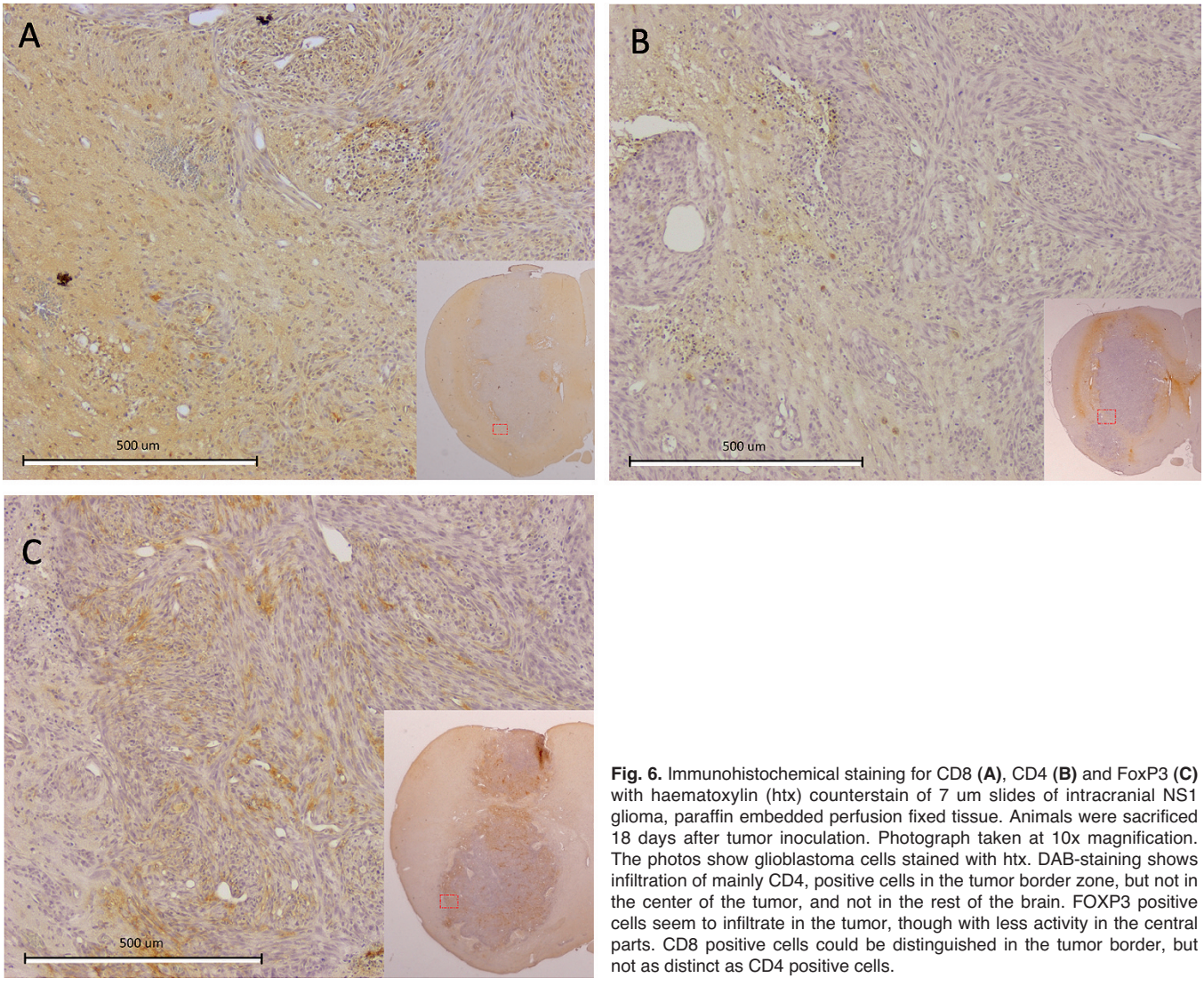

Fig. 6. Immunohistochemical staining for CD8 **(A)**, CD4 **(B)** and FoxP3 **(C)** with haematoxylin (htx) counterstain of 7 um slides of intracranial NS1 glioma, paraffin embedded perfusion fixed tissue. Animals were sacrificed 18 days after tumor inoculation. Photograph taken at 10x magnification. The photos show glioblastoma cells stained with htx. DAB-staining shows infiltration of mainly CD4, positive cells in the tumor border zone, but not in the center of the tumor, and not in the rest of the brain. FOXP3 positive cells seem to infiltrate in the tumor, though with less activity in the central parts. CD8 positive cells could be distinguished in the tumor border, but not as distinct as CD4 positive cells.

advantage of the constitutive expression of GFP by supposedly all tumor cells which in this rat model (Nittby et al., 2015) likely contain several different genomic profiles. Although it cannot be ruled out that individual tumor cells lose their GFP expression this seems unlikely since we did not encounter any GFP- cells that were, on morphological grounds, suspected to be of tumor origin – on the other hand we often noticed GFP+ cells without obvious morphological tumor characteristics but with a location and arrangement consistent with migration and proliferation.

Whilst models with specified genetic changes are obviously both useful and attractive as many fulfill the morphological criteria for glioblastoma (Ding et al., 2000; Chen et al., 2012) and have supplied much important information (Liu et al., 2011; Chen et al., 2012) they suffer in the respect that we do not know how much they resemble the human tumor (de Vries et al., 2009). In fact, specific therapy geared towards such defects has so far failed (Lau et al., 2014; Prados et al., 2015). Taken together with the absence of corresponding genetic defects in a large share of human glioblastomas, this suggests that such singular changes, when they occur, while still having the characteristics of "driver" mutations, may not be at the root of the clinical problem but could represent an effect of ensuing genomic instability and thus not represent worthwhile therapeutic targets. The present NS-1 model, which presumably contains many different genetic and epigenetic alterations, may in this respect more resemble human glioblastoma and consequently be more useful in clinically oriented research.

The demonstration of spread to and proliferation of tumor within the subventricular zone is particularly interesting in view of the notion that this area may be the origin of TICs in spontaneous tumors (Sanai et al., 2005). The high sensitivity of the method described suggest the possibility of detecting such invasion at a very early stage or, alternatively to stereotactically inject very small numbers of tumor cells within the confines of this restricted area in order to study e.g. if this location provides a selective protection against various therapeutic measures.

The results indicate that intraventricular dissemination of a low number of malignant cells may be more common than has been recognized when using less sensitive methods for detection of individual tumor cells. The finding of apparently free-floating intraventricular "spheroids" which exhibit an uncanny resemblance to tumor spheres cultured *in vitro* (Weisvald et al., 2015) also suggests a way to explore the importance of the microenvironment which is obviously quite different in the intraventricular compartment compared to the situation in the parenchyma and probably much easier to manipulate.

Correlating experimental models to the clinical

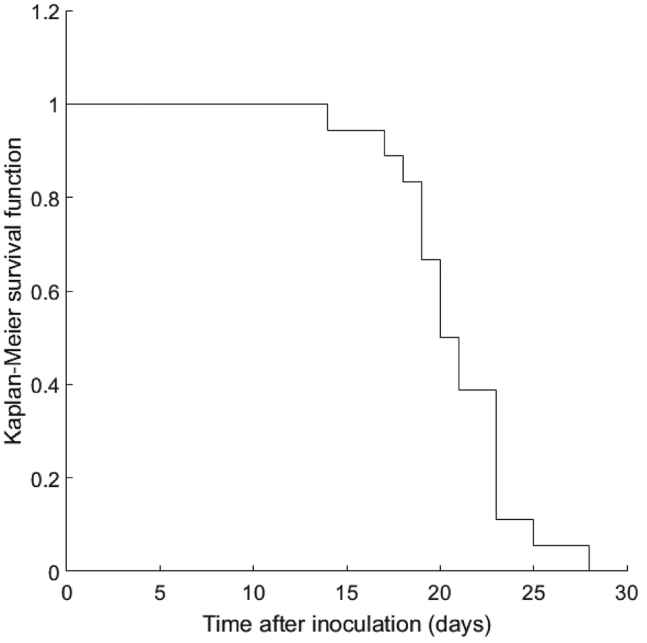

Fig. 7. Kaplan-Meier curve showing time until onset of symptoms in rats inoculated with 5000 NS1 cells.

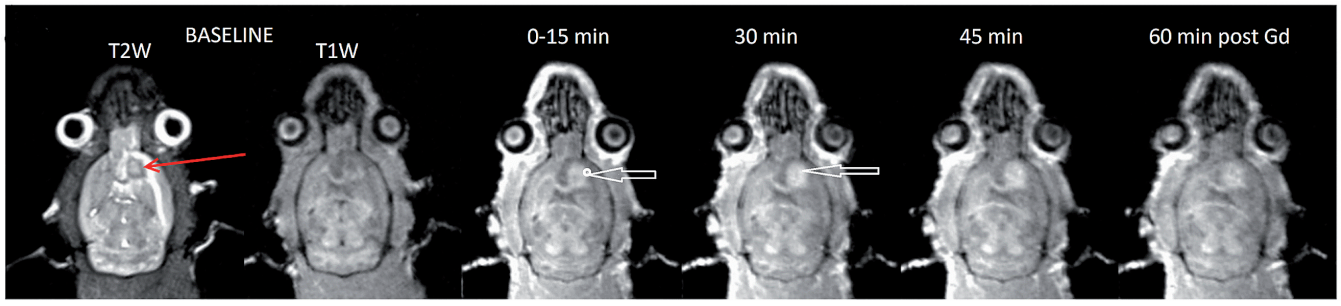

Fig. 8. Progression of MRI signal following intraperitoneal administration of contrast agent. White arrows: The diffuse bright spot (white arrow) indicates evasion of Gd contrast agent predominantly at the margin (15 mis), which is the distributed of the tumor (30min), but not into the surrounding edema (hyperintense on T2w, hypointense on T1w). The later time points indicate the clearance of Gd.

reality is not easily done. The model studied here illustrates the growth pattern of unresected glioblastoma. In the clinical setting, some patients will be candidates for resection of their glioblastoma, however, many patients will probably be more likely to undergo biopsy instead, due to the location or growth characteristics of the tumor (Müller et al., 2019). Müller et al. found a biopsy rate between 20-40%, differing between two centers; however the indication as far as location was concerned was uniform; with biopsy being the preferred treatment for tumors growing in thalamus, internal capsule, splenium of the corpus callosum, and

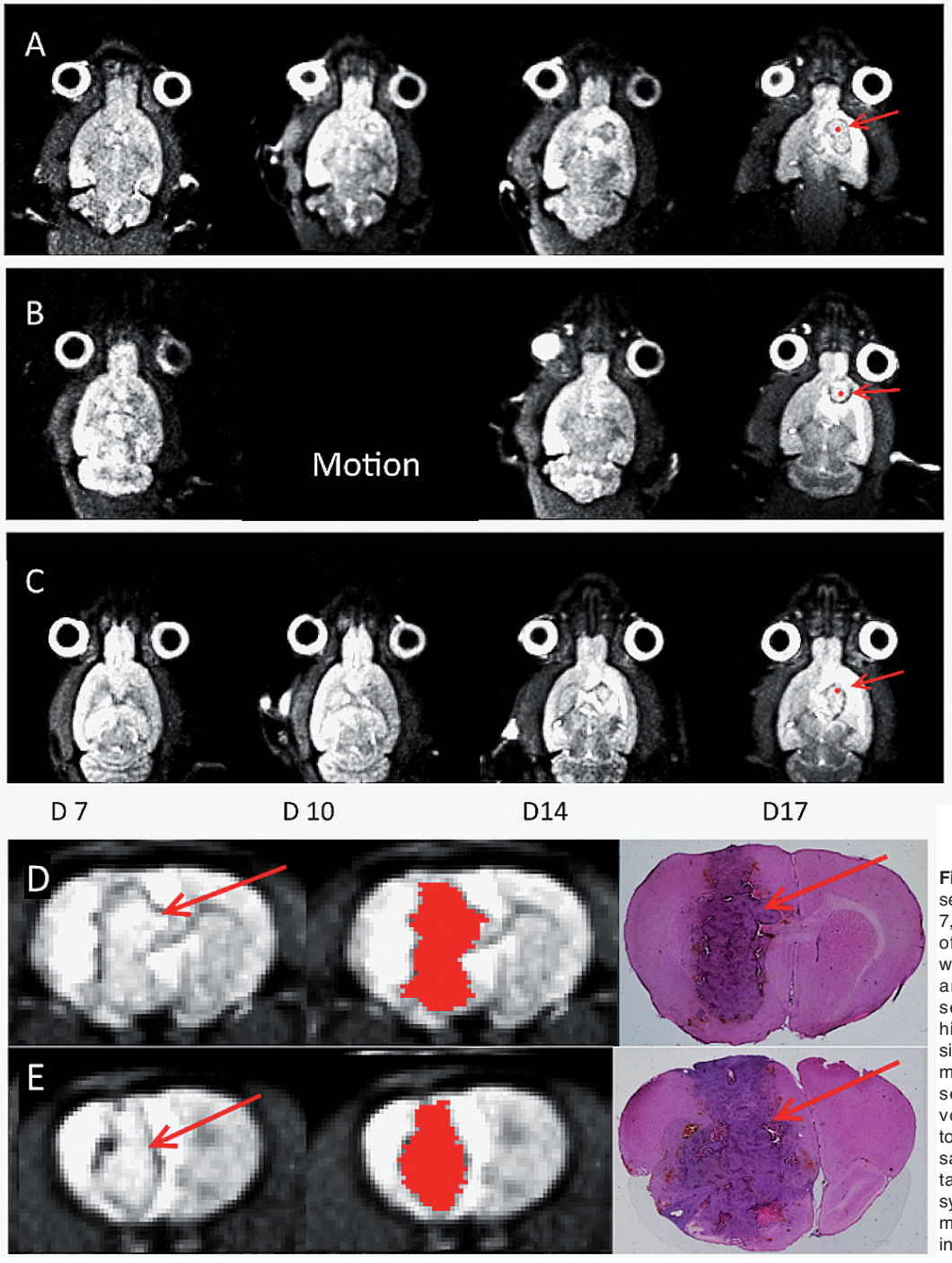

Fig. 9. A-C. Selected transverse sections of MRI images at days 7, 10, 14 and 17 after inoculation of 5000 NS1 cells. One image was excluded due to motion artifacts. D, E. MRI coronal sections and corresponding histological sections displayed side to side. Middle images show manually drawn ROI in the selected section, on which volumetry was based. The topmost rat was euthanized the same day as MRI images was taken, lowermost rat displayed symptoms two days later, which may explain the larger tumor size in the histological section.

periventricular region around the occipital horns. In the present model tumor cells are inoculated into the caudate nucleus, meaning that studying the growth pattern without resection is of relevance. Furthermore, we think that it is important to study the untreated tumor, since it has been shown that the neuro-oncological treatment offered alter the tumor, meaning that the one seen upon recurrence is not the genetically same tumor which was diagnosed initially (Neilsen et al., 2019).

Taken together, the growth properties of a highly infiltrative glioblastoma in immunocompetent animals without treatment is described in detail. One reason to

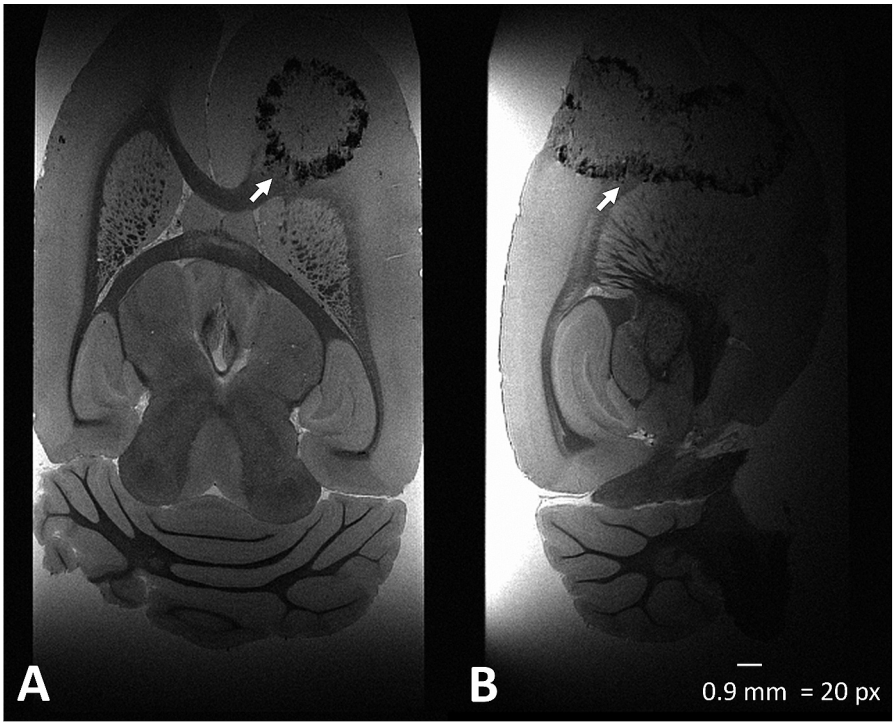

Fig. 10. T2*-weighted 3D MRI at a resolution of 45 micros of a fixed brain 14 days of inoculation of 5000 cells in axial **(A)** and sagittal **(B)** view. Arrows indicate infiltration along the corpus callosum. The intensity gradient reflects the sensitivity of the cryocoil.

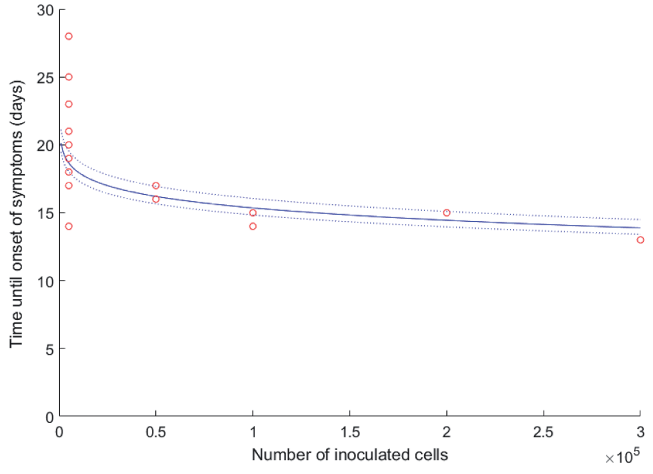

Fig. 11. Time until onset of symptoms as a function of number of inoculated cells. Red circles represent experimental data and the blue line represents the model in Equation (1). The dotted lines indicate the 2.5th and 97.5th percentiles of the model predictions.

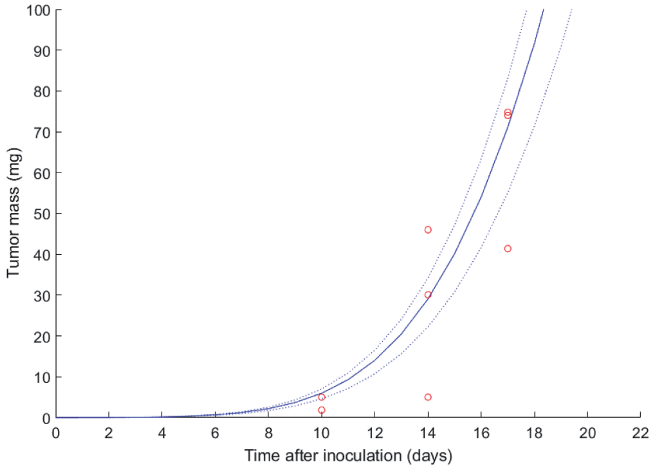

Fig. 12. Tumor mass as a function of time after inoculation of 5000 NS1 cells. Red circles represent experimental data and the blue line represents the model in Equation (1). The dotted lines indicate the 2.5th and 97.5th percentiles of the model predictions.

characterize the growth of an experimental glioblastoma model is to adjust subsequent studies to a clinically relevant setting. In particular, one should avoid initiating therapies too early after tumor inoculation, when tumor burden is much smaller than in a clinical context. The formulas presented here could be applied to other models as well, given that the relevant variables are provided.

Acknowledgements. We are grateful to the Gunnar Nilsson Cancer Foundation and the Elsa Schmitz foundation for financial support.

References

Ahlstedt J., Förnvik K., Zolfaghari S., Kwak D., Hammarström L.G.J., Ernfors P., Salford L.G. and Redebrandt H.N. (2018). Evaulating Vaquinol-1 in rats carrying glioblastoma models RG2 and NS1. Oncotarget 9, 8391-8399.

Ahmad F.T. and Malik J. (2017). Epidemiology and outcome of glioblastoma. In: Glioblastoma. De Vleeschouwer S. (ed). Brisbane (AU). Codon Publications;

Barth R.F. and Kaur B. (2009). Rat brain tumor models in experimental neuro-oncology: the C6, 9L, T9, RG2, F98, BT4C, RT-2 and CNS-1 gliomas. J. Neurooncol. 94, 299-312.

Chen J., Li Y., Yu T.S., McKay R.M., Burns D.K., Kernie S.G. and Parada L.F. (2012). A restricted cell population propagates glioblastoma growth after chemotherapy. Nature 488, 522-526.

De Vries N.A., Beijnen J.H. and van Tellingen O. (2009) High-grade glioma mouse models and their applicability for preclinical testing. Cancer Treat. Rev. 35, 714-723.

Ding H., Nagy A., Gutmann D.H. and Guha A. (2000). A review of astrocytoma models. Neurosurgical Focus 8, 1-8.

Dréan A., Goldwirt L., Verreault M., Canney M., Schmitt C., Guehennec J., Delattre J.Y., Carpentier A. and Idbaih A. (2016). Blood-brain barrier, cytotoxic chemotherapies and glioblastoma. Expert Rev. Neurother. 16, 285-1300.

Duran C.L., Lee D.W., Jung J-U., Ravi S., Pogue C.B., Toussaint L.G., Bayless K.J. and Sitcheran R. (2016). NIK regulate MT1-MMP activity and promotes glioma cell invasion independently of the cnonical NF-kB-pathway. Oncogenesis 5, 1-12

Endaya B.B., Lam P.Y., Meedeniya A.C. and Neuzil J. (2016). Transcriptional profiling of dividing tumor cells detects intratumor heterogeneity linked to cell proliferation in a brain tumor model. Mol. Oncol. 10, 126-137.

Förnvik K., Maddahi A., Persson O., Osther K., Salford L.G. and Nittby Redebrandt H. (2017). C1-Inactivator is Upregulated in Glioblastoma. PLoS One 12, e0183086.

Hambardzumyan D., Gutmann D.H. and Kettenmann H. (2016). The role of microglia and macrophages in glioma maintenance and progression. Nat. Neurosci. 19, 20-27.

Helms G., Garea-Rodriguez E., Schlumbohm C., König J., Dechent P., Fuchs E. and Wilke M. (2013). Structural and quantitative neuroimaging of the common marmoset monkey using a clinical MRI system. J. Neurosci. Methods 215, 121-131.

Hoffman R. (2015). Application of GFP imaging in cancer. Lab. Invest. 95, 432-452.

Jack C.R., Bernstein M.A., Fox N.C., Thompson P., Alexander G., Harvey D., Borowski B., Britson P.J., L Whitwell J., Ward C., Dale A.M., Felmlee J.P., Gunter J.L., Hill D.L., Killiany R., Schuff N., Fox-Bosetti S., Lin C., Studholme C., DeCarli C.S., Krueger G., Ward H.A., Metzger G.J., Scott K.T., Mallozzi R., Blezek D., Levy J., Debbins J.P., Fleisher A.S., Albert M., Green R., Bartzokis G., Glover G., Mugler J. and Weiner M.W. (2008). The Alzheimer's Disease Neuroimaging Initiative (ADNI): MRI methods. J. Magn. Reson. Imaging. 27, 685-691.

Kijima N. and Kanemura Y. (2017). Mouse models of glioblastoma. In: Glioblastoma. De Vleeschouwer S. (ed). Brisbane (AU): Codon Publications.

Lampson L.A. (2013). Brain tumor models to predict clinical outcome: Like the phoenix?. In: Animal models of brain tumors. Martínez Murillo R. and Martínez A. (eds). Neuromethods, vol 77. Humana Press, Totowa, NJ.

Lau D., Magill S.T. and Aghi M. (2014). Molecularly targeted therapies for recurrent glioblastoma: current and future targets. Neurosurg. Focus 37, 1-21.

Liu C., Sage J.C., Miller M.R., Verhaak R.G., Hippenmeyer S., Vogel H., Foreman O., Bronson R.T., Nishiyama A., Luo L. and Zong H. (2011). Mosaic analysis with double markers reveals tumor cell of origin in glioma. Cell 146, 209-221.

Marumoto T., Tashiro A., Friedmann-Morvinski D., Scadeng M., Soda Y., Gage F.H. and Verma I.M. (2009). Development of a novel mouse glioma model using lentiviral vectors. Nat. Med. 15, 110-116.

Mc Lendon R.E., Rosenblum M.K. and Bigner D.D. (1998). Russel and Rubinstein´s pathology of tumors of the nervous system. Arnold. London. Vol. 1-2.

Müller D.M.J., Robe P.A.J.T., Eijgelaar R.S., Witte M.G., Visser M., de Munck J.C., Broekman M.L.D., Seute T., Hendrikse J., Noske D.P., Vandertop W.P., Barkhof F., Kouwenhoven M.C.M., Mandonnet E., Berger M.S. and De Witt Hamer P.C. (2019). Comparing glioblastoma surgery decisions between teams using brain maps of tumor locations, biopsies, and resections. JCO Clin. Cancer. Inform. 3, 1-12.

Neilsen B.K., Sleightholm R., McComb R., Ramkissoon SH., Ross J.S., Corona R.J., Miller V.A., Cooke M. and Aizenberg M.R. (2019). Comprehensive genetic alteration profiling in primary and recurrent glioblastoma. J. Neurooncol. 142, 111-118.

Nittby H., Förnvik K., Ahlstedt J., Ceberg C., Ericsson P., Persson B.R., Skagerberg G., Widegren B., Xue Z. and Salford L.G. (2015). A GFP positive glioblastoma cell line NS1 – a new tool for experimental studies. Brain Tumors Neurooncol. 1, 1-8.

Ohgaki H. and P. Kleihues. (2005). Epidemiology and etiology of gliomas. Acta Neuropathol. 109, 93-108.

Prados M.D., Byron S.A., Tran N.L., Phillips J.J., Molinaro A.M., Ligon K.L., Wen P.Y., Kuhn J.G., Mellinghoff I.K., de Groot J.F., Colman H., Cloughesy T.F., Chang S.M., Ryken T.C., Tembe W.D., Kiefer J.A., Berens M.E., Craig D.W., Carpten J.D. and Trent J.M. (2015). Toward precision medicine in glioblastoma: the promise and challenges. Neuro. Oncol. 17, 10511-1063.

Rutter E.M., Stepien T.L., Anderies B.J., Plasencia J.D., Woolf E.C., Scheck A.C., Turner G.H., Liu Q., Frakes D., Kodibagkar V., Kuang Y., Preul M.C. and Kostelich E.J. (2017). Mathematical analysis of glioma growth in a murine model. Sci. Rep. 7, 4-16.

Sanai N., Alvarez-Buylla A. and Berger M.S. (2005). Neural stem cells and the origin of gliomas. N. Engl. J. Med. 353, 811-821.

Sourbron S.P. and Buckley D.L. (2013). Classic models for dynamic contrast-enhanced MRI. NMR Biomed. 26, 1004-1027.

Stensjoen A.L., Berntsen E.M., Jakola A.S. and Solheim O. (2018). When did the glioblastoma start growing, and how much time can be gained from surgical resection? A model based on the pattern of glioblastoma growth *in vivo*. Clin. Neurol. Neurosurg. 170, 38-42.

Stylli S.S., Luwor R.B., Ware T.M.B., Tand F. and Kaye A.H. (2015). Mouse models of glioma. J. Clin. Neuroscience 22, 619-626.

Tamase A., Muraguchi T., Naka K., Tanaka S., Kinoshita M., Hoshii T., Ohmura M., Shugo H., Ooshio T., Nakada M., Sawamoto K., Onodera M., Matsumoto K., Oshima M., Asano M., Saya H., Okano H., Suda T., Hamada J. and Hirao A (2009). Identification of tumor-initiating cells in a highly aggressive brain tumor using promoter activity of nucleostemin. Proc. Natl. Acad. Sci. USA 106, 17163-17168.

Tjørve K.M.C. and Tjørve E. (2017). The use of Gompertz models in growth analyses, and new Gompertz-model approach: An addition to the Unified-Richards family. PLoS One 12. e0178691.

Accepted February 5, 2020